Fusion enhancement in the collisions with ^{44}Ca beams and the production of neutron-deficient $^{245–250}$Lr isotopes

Li-Lin Zhou,[1] Jun-Jun Cai,[1] Lu-Qi Li,[2] Zi-Long Wang,[1] Rui Zhu,[1] Xiao-Ye Zhang,[1] Xin-Rui Zhang,[3] Long Zhu,[4,5] Gen Zhang,[1,*] and Feng-Shou Zhang[6,7,8]

[1]*Guangxi Key Laboratory for Relativistic Astrophysics, School of Physical Science and Technology, Guangxi University, Nanning 530004, China*

[2]*China Institute of Atomic Energy, Beijing 102413, China*

[3]*Guangxi Normal University, College of Physical Science and Technology, Guilin 541004, China*

[4]*Sino-French Institute of Nuclear Engineering and Technology, Sun Yat-sen, University, Zhuhai 519082, China*

[5]*Guangxi Key Laboratory of Nuclear Physics and Nuclear Technology, Guangxi Normal, University, Guilin 541004, China*

[6]*The Key Laboratory of Beam Technology of Ministry of Education, College of Nuclear Science and Technology, Beijing Normal University, Beijing 100875, China*

[7]*Institute of Radiation Technology, Beijing Academy of Science and Technology, Beijing 100875, China*

[8]*Center of Theoretical Nuclear Physics, National Laboratory of Heavy Ion Accelerator of Lanzhou, Lanzhou 730000, China*

(Received 28 November 2023; accepted 22 January 2024; published 13 February 2024)

Within the framework of the isospin-dependent quantum molecular dynamics model and statistical evaporation model, the production of neutron-deficient $^{245–250}$Lr isotopes is investigated. The fusion probability in the reaction ^{44}Ca + ^{209}Bi is larger than that with ^{40}Ca beam, especially at a lower incident energy and smaller impact parameter, which is attributed to a lower dynamical barrier in ^{44}Ca + ^{209}Bi. The neck between the projectile and target grows faster in the reaction with ^{44}Ca beam, and the N/Z ratio in the neck is larger, resulting in a lower dynamical barrier. Based on the fusion reactions of ^{40,44}Ca + ^{209}Bi and ^{46,48}Ti + ^{203}Tl, we predicted six new Lr isotopes, $^{245–250}$Lr, with the maximal evaporation residue cross sections of 3.5 fb, 69 pb, 0.2 nb, 0.4 nb, 1.7 nb, and 1.8 nb, respectively.

DOI: 10.1103/PhysRevC.109.024606

I. INTRODUCTION

The synthesis of superheavy nuclei (SHN) is one of the most significant challenges in low-energy nuclear physics. Over the past three decades, through systematic experimental efforts, elements up to oganesson with $Z = 118$ have been discovered, completing the seventh row of the periodic table [1–5]. Both hot and cold fusion reactions have been extensively and effectively employed to produce SHN [6–17]. The discovery of new isotopes near the proton drip line can offer valuable insights into the nuclear structure and properties, as well as reveal the boundary behavior of nuclear systems [24]. The unique characteristics, including the novel decay modes, halo structure, and shell evolution have been observed in that region [18–20].

For instance, the odd-odd nuclei ^{236}Bk, ^{240}Es, and ^{244}Md near the proton drip line offer avenues for exploring β and electron-capture delayed fission [21–23], thereby providing new insights into the low-energy spontaneous fission processes. The proton $1/2^-[521]$ Nilsson orbits, originating from the $f_{5/2}$ spherical orbit above the $Z = 114$ shell gap, have been found near the ground states of neutron-deficient isotopes of Md, Lr, and Db [25]. However, the relative energy of this orbit can only be determined from ^{255}Lr and its decay products [26]. Up to date, a total of 14 Lr isotopes have been discovered [16,27–35]. The element Lawrencium ($Z = 103$) was first discovered by Ghiorso *et al.* in 1961 [31]. The isotopes ^{255,256}Lr were successfully detected through the complete fusion reactions of ^{16,18}O + ^{243}Am at Dubna [36,37]. The isotopes $^{257–260}$Lr were synthesized using hot fusion reactions with ^{15}N or ^{18}O beam [33], while the multinucleon transfer reactions ^{22}Ne + ^{254}Es were conducted to produce ^{261,262}Lr at Berkeley [38,39]. Last year, Oganessian *et al.* discovered ^{264}Lr in the decay chain of ^{268}Db [35]. Shortly thereafter, Huang *et al.* found a new isotope, ^{251}Lr, with the reaction ^{203}Tl(^{50}Ti, $2n$)^{251}Lr [27]. Meanwhile, through the cold fusion reactions of ^{50}Ti + ^{209}Bi and ^{54}Cr + ^{209}Bi, $^{252–254}$Lr were identified utilizing the velocity filter SHIP at GSI [29,40,41]. The most Lr isotopes were synthesized via fusion-evaporation reactions, except the isotopes ^{261,262}Lr. All experimentally produced Lr isotopes are neutron-deficient, but not approaching the proton drip line so far.

Various theoretical models have been developed to describe low-energy fusion reactions. Microscopic dynamical models, such as isospin-dependent quantum molecular dynamics (IQMD) model [42,43] and time-dependent Hartree-Fock model [44–46], have shown reasonable success in investigating the dynamical mechanism in heavy-ion collisions. Additionally, semiclassical models such as the two-step model [47], the dinuclear system (DNS) model [48–51], and

*Corresponding author: zhanggen@gxu.edu.cn

Langevin equation [52–54] have been utilized to predict the production cross sections of SHN. IQMD model is a transport model that not only incorporates mean-field effects but also introduces two-body collisions and Pauli blocking [55]. That model has been applied widely to describe neck dynamics and production mechanism of heavy nuclei in fusion reactions [56,57].

The aim of this work is to search for the optimal projectile-target combinations to synthesize unknown neutron-deficient Lr isotopes. The reactions $^{40,44}\mathrm{Ca} + {}^{209}\mathrm{Bi}$ and $^{46,48}\mathrm{Ti} + {}^{203,205}\mathrm{Tl}$ are chosen to produce these isotopes with the goal of determining the optimal incident energy and evaporation residue cross section (ER) of the new Lr isotopes.

The structure of this article is organized as follows. In Sec. II, we introduce the IQMD and statistical evaporation model briefly. The results and discussions are presented in Sec. III. The conclusion is given in Sec. IV.

II. MODEL

In the IQMD model, as in the original QMD model [58], each nucleon is represented by a coherent state of Gaussian wave packets,

$$\phi_i(\mathbf{r}) = \frac{1}{(2\pi\sigma_r^2)^{3/4}} \exp\left[-\frac{(\mathbf{r}-\mathbf{r}_i)^2}{4\sigma_r^2} + \frac{i}{\hbar}\mathbf{r}\cdot\mathbf{p}_i\right]. \tag{1}$$

Here, $\mathbf{r}_i$ and $\mathbf{p}_i$ represent the centers of the ith wave packet in coordinate space and momentum space, respectively. σ_r is the width of the wave packet in coordinate space [59]. In order to reduce computational complexity, the n-body wave function of the entire system is taken as the direct product of the coherent states,

$$\Phi(\mathbf{r}, t) = \prod_i \phi_i(\mathbf{r}, \mathbf{r}_i, \mathbf{p}_i, t). \tag{2}$$

We consider the width of the wave packet depends on the system size, which is expressed as

$$\sigma_r = 0.09A^{1/3} + 0.88. \tag{3}$$

By utilizing the Wigner transformation, one can derive the density and momentum distributions of a given system:

$$\rho(\mathbf{r}) = \sum_i \frac{1}{(2\pi\sigma_r^2)^{3/2}} \exp\left[-\frac{(\mathbf{r}-\mathbf{r}_i)^2}{2\sigma_r^2}\right], \tag{4}$$

$$\mathrm{g}(\mathbf{p}) = \sum_i \frac{1}{(2\pi\sigma_p^2)^{3/2}} \exp\left[-\frac{(\mathbf{p}-\mathbf{p}_i)^2}{2\sigma_p^2}\right]. \tag{5}$$

The time evolution of the coordinate and momentum of the nucleons is subject to Hamiltonian equations of motion:

$$\dot{\mathbf{r}}_i = \frac{\partial H}{\partial \mathbf{p}_i}, \quad \dot{\mathbf{p}}_i = -\frac{\partial H}{\partial \mathbf{r}_i}. \tag{6}$$

The Hamiltonian H is composed of the kinetic energy $T = \sum_i p_i^2/2m$ and the effective interaction potential,

$$H = T + U. \tag{7}$$

The effective interaction potential comprises volume, symmetry, surface, effective mass, and Coulomb terms, which are calculated by the following expressions:

$$U_{\mathrm{vol}} = \frac{\alpha}{2}\sum_i\sum_{j\neq i}\frac{\rho_{ij}}{\rho_0} + \frac{\beta}{1+\gamma}\sum_i\left(\sum_{i\neq j}\frac{\rho_{ij}}{\rho_0}\right)^{\gamma}, \tag{8}$$

$$U_{\mathrm{sym}} = \frac{C_{\mathrm{sym}}}{2}\sum_i\sum_{j\neq i} t_{iz}t_{jz}\frac{\rho_{ij}}{\rho_0} \times\left(1 - k_{\mathrm{sym}}\left[\frac{3}{2\sigma_r^2} - \left(\frac{\mathbf{r}_i-\mathbf{r}_j}{2\sigma_r^2}\right)^2\right]\right), \tag{9}$$

$$U_{\mathrm{surf}} = \frac{g_{\mathrm{surf}}}{2}\sum_i\sum_{j\neq i}\left[\frac{3}{2\sigma_r^2} - \left(\frac{\mathbf{r}_i-\mathbf{r}_j}{2\sigma_r^2}\right)^2\right]\frac{\rho_{ij}}{\rho_0}, \tag{10}$$

$$U_{\mathrm{eff}} = g_\tau\sum_i\left(\sum_{i\neq j}\frac{\rho_{ij}}{\rho_0}\right)^{\eta}, \tag{11}$$

$$U_{\mathrm{Coul}} = \frac{e^2}{4\pi\epsilon_0}\sum_i\sum_{j\neq i}\frac{1}{r_{ij}}(1+t_{iz})(1+t_{jz})\,\mathrm{erf}\left(\frac{r_{ij}}{\sqrt{4\sigma_r^2}}\right) + C_{\mathrm{ex}}\sum_i\left[\sum_{j\neq i} t_{iz}t_{jz}\rho_{ij}\right]^{1/3}, \tag{12}$$

where

$$\rho_{ij} = \frac{1}{(4\pi\sigma_{\mathrm{r}}^2)^{3/2}}\exp\left(-\frac{r_{ij}^2}{4\sigma_{\mathrm{r}}^2}\right). \tag{13}$$

To improve the nucleon's fermionic nature, the phase space occupation constraint is adopted, proposed by Papa *et al.* [60]. The occupancy rate $\overline{f_i}$ in the phase space volume h^3 around nucleon i is defined as

$$\overline{f_i} = \sum_j \delta_{\tau_i\tau_j}\delta_{s_is_j}\int_{h^3} f_j(\mathbf{r}, \mathbf{p}, t)d^3r d^3p. \tag{14}$$

Here, s_i and τ_i represent the projection quantum numbers of the spin and isospin of nucleon i, respectively.

The fusion cross section is obtained by integrating the fusion probability over a certain impact parameter range with this formula [61]

$$\sigma_{\mathrm{fus}}(E_{\mathrm{c.m.}}) = 2\pi\sum b g_{\mathrm{fus}}(E_{\mathrm{c.m.}}, b)\Delta b. \tag{15}$$

Here, g_{fus} represents the fusion probability at impact parameter b and incident energy $E_{\mathrm{c.m.}}$. The fusion probability is obtained by counting the number of fusion event under a large number of simulated events.

In this work, we adopt the parameter IQ2 (see Table I), with the z axis aligned along the beam direction and the x axis aligned along the collision parameter direction [55,61]. The dynamical simulations are terminated at 1000 fm/c.

The de-excitation process of the compound nucleus is investigated by the statistical evaporation model. The ER cross section of SHN is calculated by the formula [48]

$$\sigma_{\mathrm{ER}}(E_{\mathrm{c.m.}}, J) = \sigma_{\mathrm{fus}}(E_{\mathrm{c.m.}}, J)W_{\mathrm{sur}}(E_{\mathrm{c.m.}}, J), \tag{16}$$

TABLE I. Model parameters (IQ2) adopted in this work.

α (MeV)	β (MeV)	γ	g_{sur} (MeV fm^2)	g_τ (MeV)	η	C_s (MeV)	κ_s(fm^2)	ρ_0 (fm^{-3})
-356	303	7/6	7.0	12.5	2/3	32	0.08	0.165

where W_{sur} represents the survival probability of the SHN. Taking into account the competition between neutron evaporation and fission, the survival probability of the SHN after evaporating x ($x > 1$) neutrons can be written as follows:

$$W_{sur}(E^*_{CN}, x, J) = P(E^*_{CN}, x, J)\prod_{i=1}^{x}\frac{\Gamma_n(E^*_i, J)}{\Gamma_n(E^*_i, J) + \Gamma_f(E^*_i, J)}. \tag{17}$$

Here, E^*_{CN} and J denote the excitation energy and angular momentum of the compound nucleus, respectively. Γ_n and Γ_f are the neutron evaporation width and fission width, which can be calculated by Weisskopf's evaporation theory [62] and Bohr-Wheeler formula, respectively [63]. E^*_i is the excitation energy of the SHN before evaporating the ith neutron, which can be expressed as follows:

$$E^*_{i+1} = E^*_i - B^n_i - 2T_i. \tag{18}$$

Here, B^n_i represents the separation energy of the ith neutron. The nuclear temperature T_i before evaporating the ith neutron is given by the relation

$$E^*_i = aT_i^2 - 2T_i. \tag{19}$$

In this work, we use a macroscopic liquid drop model with microscopic shell correction to calculate the fission barrier B_f. The fission barrier with an excitation energy-dependent shell correction is expressed in the following form:

$$B_f = B_f^{LD} + B_f^M(E^* = 0)e^{-E^*/E_D}, \tag{20}$$

where E_D denotes the shell damping factor. The macroscopic part B_f^{LD} can be calculated using the liquid drop model [64]

$$B_f^{LD} = \begin{cases} 0.38(0.75 - x)E_{s0} & (1/3 < x < 2/3) \\ 0.83(1 - x)^3 E_{s0} & (2/3 < x < 1) \end{cases}. \tag{21}$$

Here, the fissility parameter x can be expressed as

$$x = \frac{E_{c0}}{2E_{s0}}. \tag{22}$$

Here, E_{c0} and E_{s0} represent the surface energy and Coulomb energy of a spherical nucleus, respectively, which are determined by Myers-Swiatecki mass formula [65]

$$E_{s0} = 17.944\left[1 - 1.7826\left(\frac{N-Z}{A}\right)^2\right]A^{2/3}, \tag{23}$$

$$E_{c0} = 0.7053\frac{Z^2}{A^{1/3}}. \tag{24}$$

III. RESULTS AND DISCUSSION

To verify the reliability of the IQMD model and the statistical evaporation model, the calculated fusion and ER cross sections in several reactions were compared with the experimental ones. As shown in Fig. 1, the fusion cross sections were calculated in the reactions ^{16}O + ^{238}U, ^{40,48}Ca + ^{208}Pb, and ^{84}Kr + ^{165}Ho with the compound nuclei around $Z = 103$. One can find that the calculated results reproduce the experimental data very well in both cold and hot fusion reactions. In Fig. 2, the ER cross sections in ^{48}Ca + ^{208}Pb and ^{48}Ca + ^{209}Bi reactions are presented, and the calculated results show good agreements with experimental data. It can be observed that as the excitation energy increases, more neutrons can be evaporated, and the maximal ER cross section in the $2n$ channel is larger than that in the $3n$ channel.

In order to analyze the impact of the isospin of the projectile on the fusion process, we calculated the fusion cross sections in ^{40,44}Ca + ^{209}Bi reactions, shown in Fig. 3(a). One can find that the fusion cross sections in the ^{44}Ca + ^{209}Bi reaction are larger than those in the reaction ^{40}Ca + ^{209}Bi, especially in the region below the Coulomb barrier. To further investigate the enhancement of the fusion cross sections induced by the ^{44}Ca beam, we compared the static interaction potential in both reactions, presented in Fig. 3(b). It can be observed that the static barriers in the ^{44}Ca + ^{209}Bi and ^{40}Ca + ^{209}Bi systems are 174.86 MeV and 186.02 MeV, respectively, hence the static barrier in ^{44}Ca + ^{209}Bi system is lower than that in the latter reaction. Additionally, the barrier width of ^{44}Ca + ^{209}Bi system is narrower compared to the ^{40}Ca + ^{209}Bi system, that makes it easier for the former to overcome the Coulomb barrier, leading to a higher fusion probability. As a result, compared to the ^{40}Ca + ^{209}Bi reaction, the fusion cross section below the barrier in the ^{44}Ca + ^{209}Bi system is enhanced. To investigate the fusion mechanism at different impact parameters, the fusion probability as a function of the impact parameter in the reactions ^{40,44}Ca + ^{209}Bi is calculated, displayed in Fig. 4. It can be seen that the fusion probability gradually decreases with the increase of the impact parameter at a certain energy. That is due to the increased elastic scattering probability in peripheral collisions compared to central collisions. In addition, it can be observed that the fusion probability in the reaction with ^{44}Ca beam is significantly enhanced compared to the ^{40}Ca + ^{209}Bi system at the central collision, which is particularly evident at a lower incident energy. As the incident energy increases from 175 MeV to 190 MeV, the fusion probability is significantly enhanced at peripheral collision. These results suggest that the fusion reactions with a high incident energy and a neutron-rich beam are more favorable for the formation of compound nuclei.

Considering that the nucleon density evolves with the reaction time, the interaction potential between projectile and target is dynamical. In Fig. 5, we calculated the dynamical interaction potential in ^{40,44}Ca + ^{209}Bi reactions at different incident energies. It is evident that the dynamical fusion barrier becomes higher with increasing incident energy. At a higher incident energy, not all of the kinetic energy is

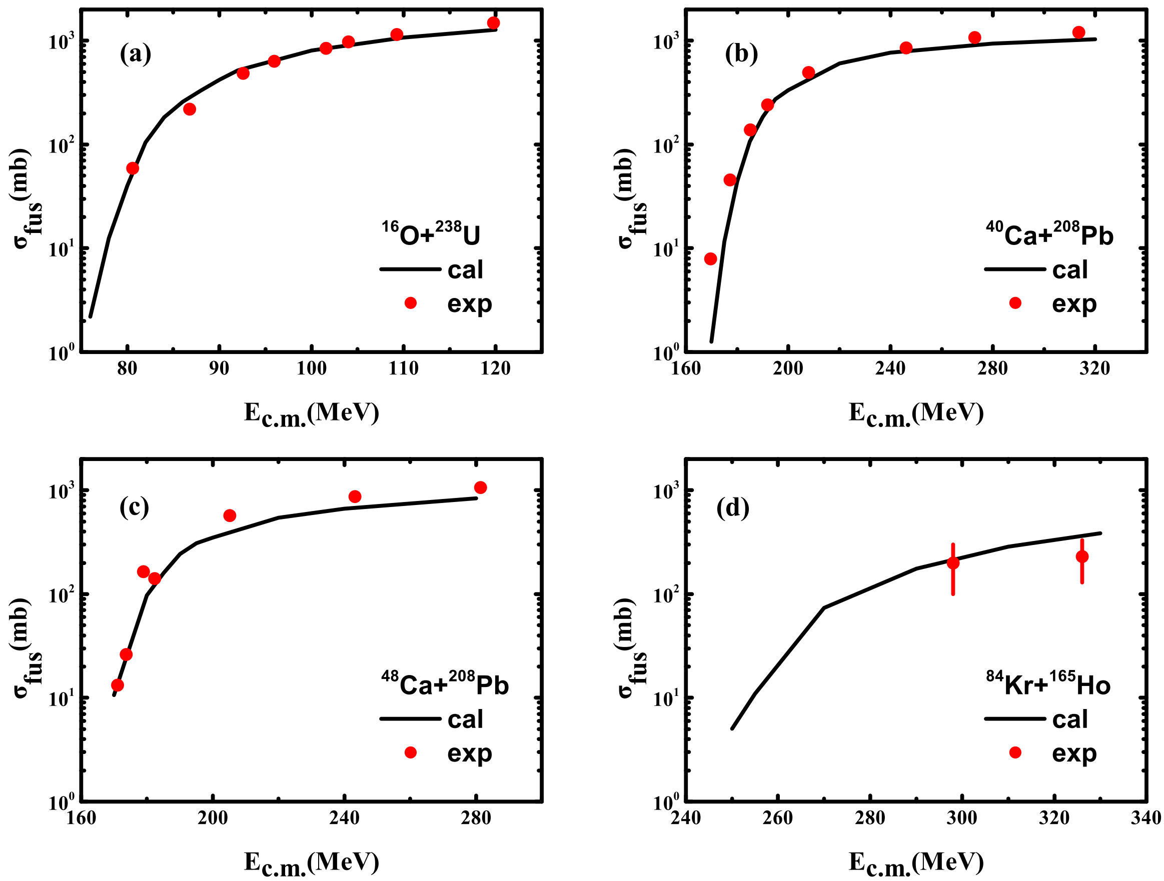

FIG. 1. Comparisons of calculated fusion cross sections with the experimental data in $^{16}O + ^{238}U$, $^{40}Ca + ^{208}Pb$, $^{48}Ca + ^{208}Pb$, and $^{84}Kr + ^{165}Ho$ reactions. The solid lines represent the calculated fusion cross sections and the circles denote the experimental data, which are obtained from Refs. [66–68].

converted into internal excitation energy of the composite system, and there is still some relative motion between the two colliding nuclei. Hence, the interaction time between two nuclei is less than the relaxation time, and the densities of the two nuclei cannot adjust in time to reach the lowest potential. As a result, the dynamical barrier becomes higher at a higher incident energy. It can be seen that the fusion barrier in $^{44}Ca + ^{209}Bi$ is lower than that in $^{40}Ca + ^{209}Bi$ at $E_{c.m.} = 180$ and 190 MeV. That makes the $^{44}Ca + ^{209}Bi$ system more likely to penetrate the barrier than the $^{40}Ca + ^{209}Bi$ system at a low energy.

The neck dynamics is crucial to understand the lowering of dynamical barrier. The evolution of the N/Z ratio in the neck in the reaction $^{40,44}Ca + ^{209}Bi$ at $E_{c.m.} = 180$ MeV

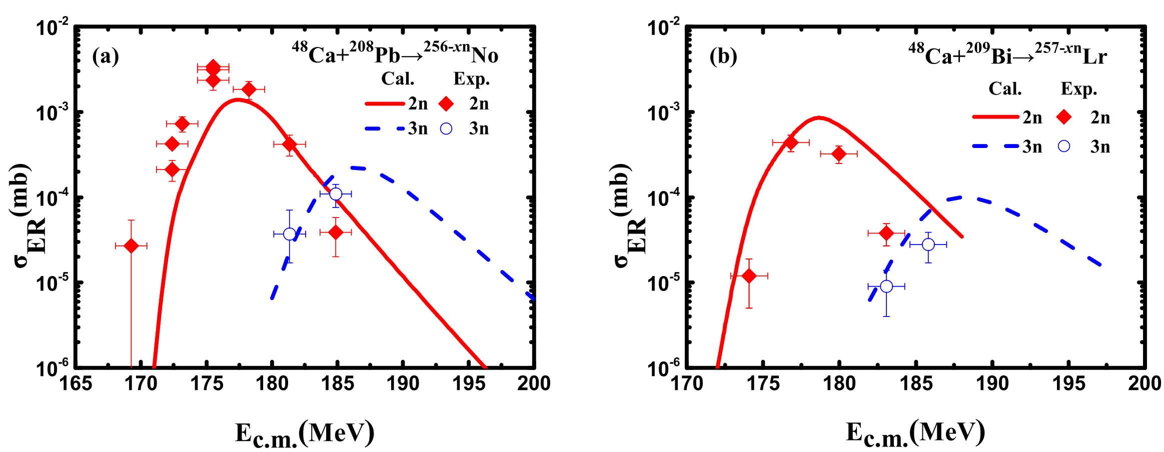

FIG. 2. The ER cross sections in the $^{48}Ca + ^{208}Pb$ and $^{48}Ca + ^{209}Bi$ reactions. The solid and dashed lines indicate calculated results in $2n$ and $3n$ channels, respectively. The diamonds and circles represent the experimental data [69] in $2n$ and $3n$ channels, respectively.

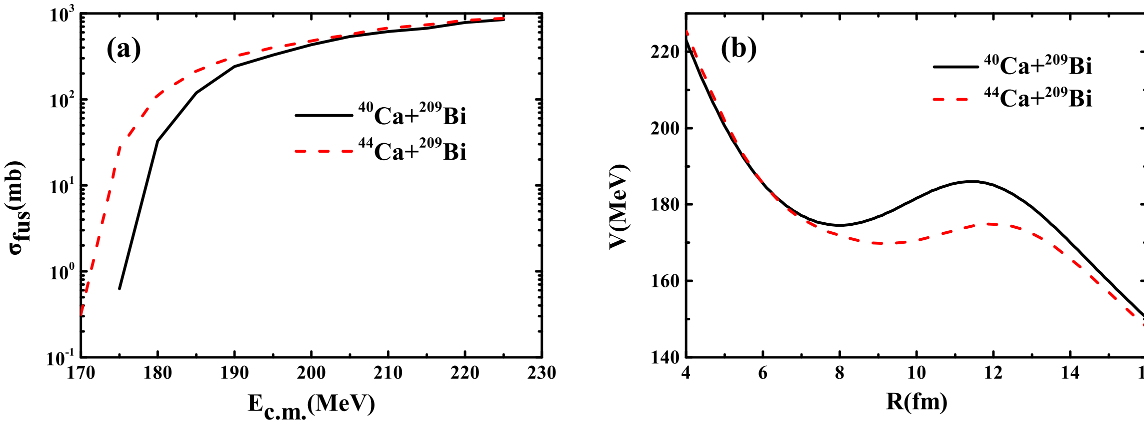

FIG. 3. (a) The fusion excitation functions in $^{40,44}\mathrm{Ca} + {}^{209}\mathrm{Bi}$ reactions denoted by the solid and dashed lines, respectively. (b) The static interaction potential in $^{40,44}\mathrm{Ca} + {}^{209}\mathrm{Bi}$ reactions are indicated by the solid and dashed lines, respectively.

is depicted in Fig. 6(a). The evolution time starts at the stage of the neck formation. The neck region is defined as a cylindrical shape along the collision orientation extending up to 4 fm. It can be observed that the N/Z ratio first increases with time, and then gradually decreases, eventually approaching the N/Z value of the compound nucleus. The increase in the N/Z ratio is mainly caused by the interplay between the symmetry potential and Coulomb potential. The symmetry potential tends to drive the nucleons towards a symmetric distribution, causing the neutron-rich system to move the excess neutrons towards the surface of the nucleus, while the Coulomb potential causes the protons to move away from the collision axis. That leads to an increase in the N/Z ratio in the neck region. As the two nuclei overlap further with time, the number of nucleons in the neck region increases, leading to a rapid decrease in the N/Z ratio until the system

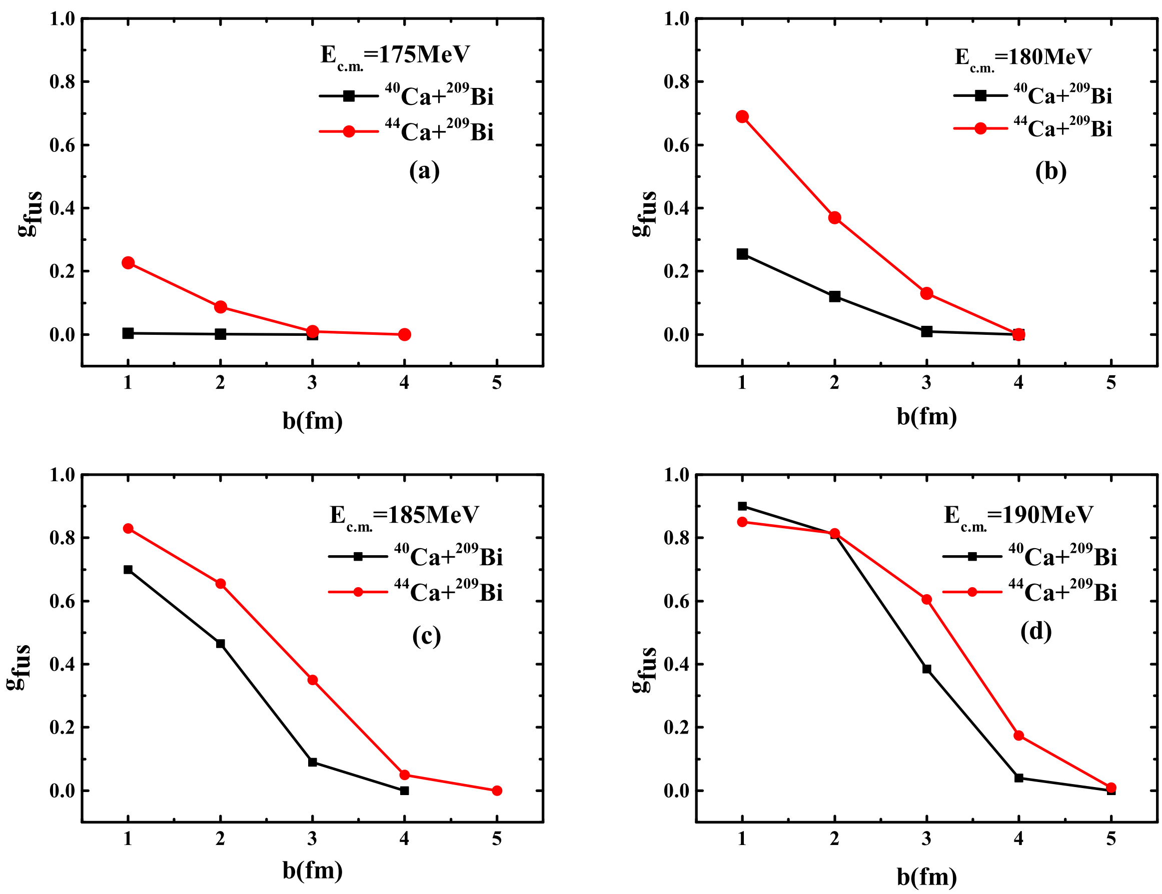

FIG. 4. Fusion probability as a function of impact parameter in $^{40,44}\mathrm{Ca} + {}^{209}\mathrm{Bi}$ reactions at $E_{\mathrm{c.m.}} = 175$, 180, 185, and 190 MeV. The square and circle symbols denote the fusion probability in $^{40}\mathrm{Ca} + {}^{209}\mathrm{Bi}$ and $^{44}\mathrm{Ca} + {}^{209}\mathrm{Bi}$, respectively.

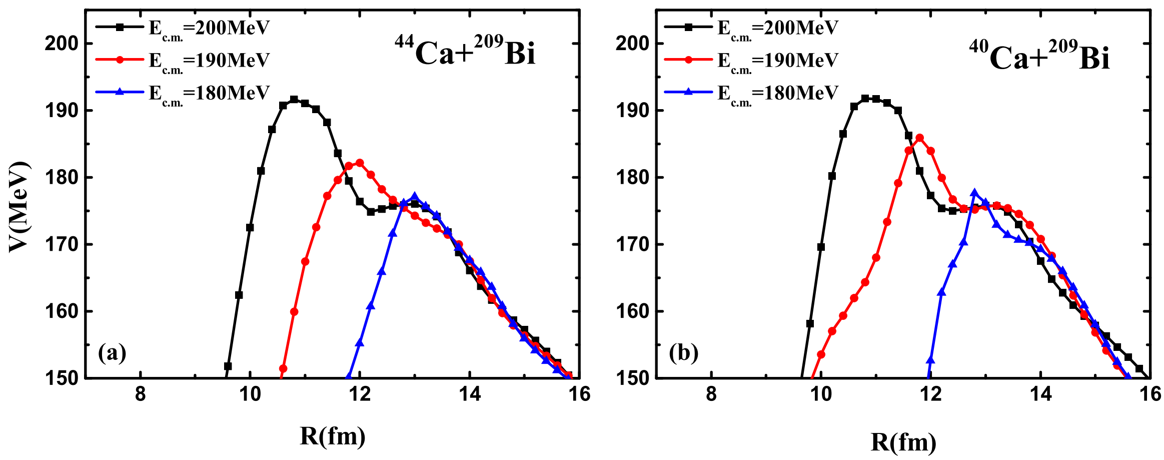

FIG. 5. The dynamical potential in the head-on collisions of $^{44}Ca + ^{209}Bi$ and $^{40}Ca + ^{209}Bi$ at $E_{c.m.} = 180$, 190, and 200 MeV, represented by the square, circle, and triangle symbols, respectively.

reaches equilibrium and forms a compound nucleus. For the system $^{44}Ca + ^{209}Bi$, the increase in the N/Z ratio after neck formation is more pronounced. The increase in the N/Z ratio can result in the dynamical lowering of the fusion barrier, thereby causing an enhancement of the fusion cross sections.

The time evolution of the radius of the neck at $E_{c.m.} = 180$ MeV are shown in Fig. 6(b). The neck radius is defined as the transverse radius along the collision direction at the central point of the neck region. It is evident that over time, the neck radius gradually increases to a maximum value, corresponding to the radius of the compound nucleus. One can find that the neck in the $^{44}Ca + ^{209}Bi$ reaction grows faster compared to the $^{40}Ca + ^{209}Bi$ reaction, which can also be applied to explain the enhancement of the fusion cross sections.

The optimal projectile-target combinations and the corresponding optimal incident energy to produce the new isotopes is significant in the experiments. Several stable projectiles and targets are selected to predict the production of new Lr isotopes. The ER cross sections in the $^{40,44}Ca + ^{209}Bi$ and $^{46,48}Ti + ^{203,205}Tl$ systems are shown in Fig. 7. The optimal reactions for the production of unknown neutron-deficient isotopes $^{245\text{–}250}Lr$ are as follows, $^{209}Bi(^{40}Ca, 4n)\,^{245}Lr$, $^{209}Bi(^{40}Ca, 3n)\,^{246}Lr$, $^{203}Tl(^{46}Ti, 2n)\,^{247}Lr$, $^{203}Tl(^{48}Ti, 3n)\,^{248}Lr$, $^{203}Tl(^{48}Ti, 2n)\,^{249}Lr$, and $^{209}Bi(^{44}Ca, 3n)\,^{250}Lr$, and the corresponding optimal incident energies are 201.7, 187, 191.5, 202.7, 193.9, and 186.8 MeV, respectively.

It can be observed that for $^{40,44}Ca + ^{209}Bi$ systems, in the same neutron evaporation channels, the maximal ER cross sections in the $^{44}Ca + ^{209}Bi$ system are significantly larger than those in the $^{40}Ca + ^{209}Bi$ system. From Fig. 4, one can find that the fusion probability in the $^{44}Ca + ^{209}Bi$ system is only a few times larger than that in the $^{40}Ca + ^{209}Bi$ system, and the enhancement of fusion probability becomes not obvious at a higher incident energy. Therefore, the significant differences in ER cross sections are mainly caused by the survival probability. Similarly, for $^{46,48}Ti + ^{203,205}Tl$ systems, the maximal ER cross sections in the $^{48}Ti + ^{205}Tl$ system are notably larger than those in the $^{48}Ti + ^{203}Tl$, $^{46}Ti + ^{205}Tl$, and $^{46}Ti + ^{203}Tl$ systems. The phenomenon can be explained as follows. The dynamical barrier in the fusion reaction with neutron-rich beam or target is reduced, leading to an increase of the fusion cross section. From the perspective of survival

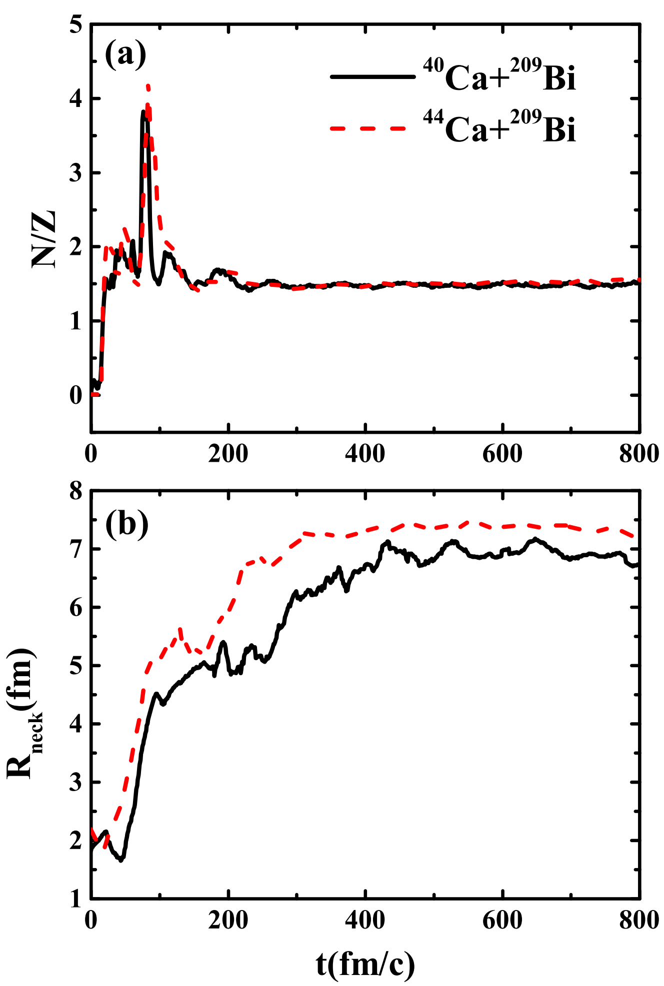

FIG. 6. (a) The N/Z ratio in the neck region and (b) the radius of the neck as functions of the evolution time at $E_{c.m.} = 180$ MeV. The solid and dashed line denote the cases of $^{40}Ca + ^{209}Bi$ and $^{44}Ca + ^{209}Bi$, respectively.

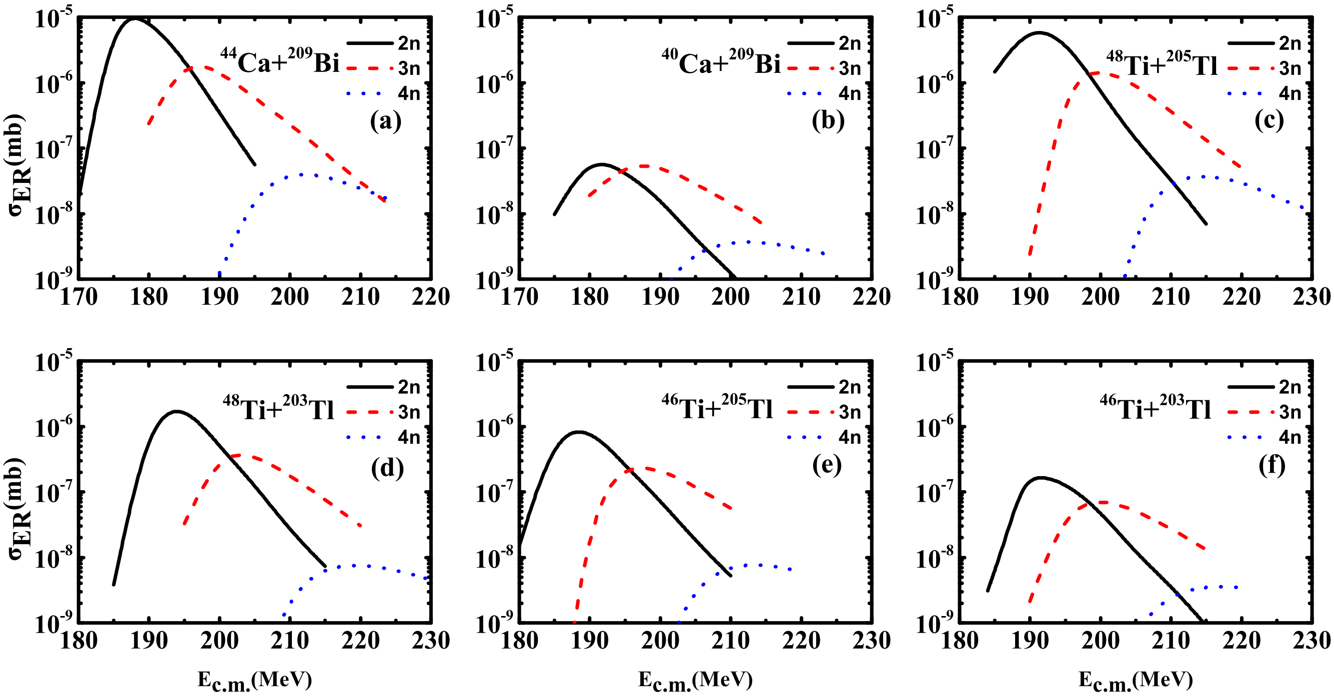

FIG. 7. The calculated ER cross sections in the reactions ^{40,44}Ca + ^{208}Pb and ^{48,46}Ti + ^{203,205}Tl. The calculated results in $2n$, $3n$, and $4n$ channels are indicated by solid, dashed, and dotted lines, respectively.

probability, it is because the fission barrier of a Lr nucleus with more neutrons is higher, resulting in a larger survival probability.

Figure 8 shows the heavy nuclei region around Lr on the nuclide chart. The filled and open squares represent discovered and predicted isotopes, respectively. The olive, yellow, blue, and red colors correspond to spontaneous fission, α decay, β^- decay, and β^+ decay, respectively. The decay properties of ^{251,264}Lr have not been measured, denoted by grey color. Six new neutron-deficient isotopes, $^{245-250}$Lr, are shown in the nuclear chart, with their maximum ER cross sections of 3.5 fb, 69 pb, 0.2 nb, 0.4 nb, 1.7 nb, and 1.8 nb, respectively.

IV. CONCLUSIONS

In summary, the production of new $^{245-250}$Lr isotopes is investigated based on the IQMD and statistical evaporation models. The calculated fusion and ER cross sections in the fusion reactions with a compound nucleus around $Z = 103$ reproduce the experimental data well. The impact of the isospin

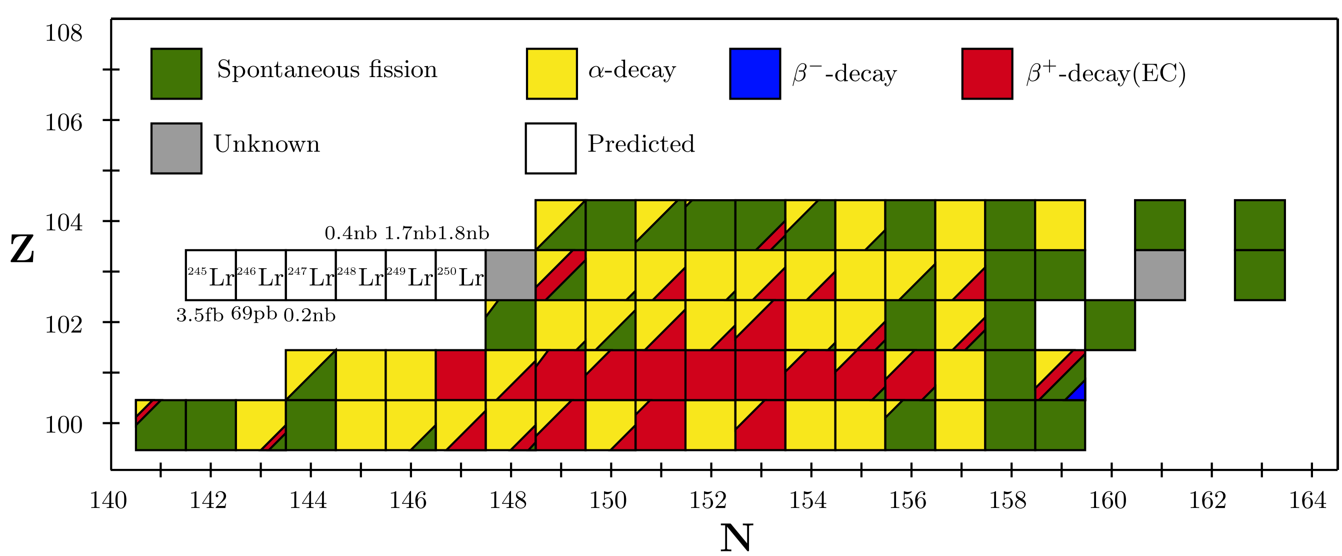

FIG. 8. Heavy nuclei region near Lr ($Z = 103$) on the nuclear map. The filled and open squares denote the known and new isotopes, respectively. Olive, yellow, blue, red, and gray colors show the spontaneous fission, α decay, β^- decay, β^+ decay, and unknown decay property, respectively. The production cross sections of the predicted Lr isotopes are indicated in the figure.

of projectile on fusion cross sections is studied. The fusion probability in $^{44}Ca + ^{209}Bi$ is larger than that in $^{40}Ca + ^{209}Bi$, especially at a lower incident energy and smaller impact parameter. That is because the dynamical barrier in $^{44}Ca + ^{209}Bi$ is lower than that in the reaction with the ^{40}Ca beam at lower incident energy. By investigating the neck dynamics in the fusion processes, it is found that the neck grows faster and the N/Z ratio is larger in $^{44}Ca + ^{209}Bi$ compared to $^{40}Ca + ^{209}Bi$, resulting in a lower barrier in $^{44}Ca + ^{209}Bi$.

By comparing the $^{40,44}Ca + ^{209}Bi$ and $^{46,48}Ti + ^{203,205}Tl$ reactions, it is evident that neutron-rich projectile-target combinations lead to an enhancement of the ER cross sections. Six new neutron-rich Lr isotopes, $^{245–250}Lr$, are predicted, with the maximal ER cross sections of 3.5 fb, 69 pb, 0.2 nb, 0.4 nb, 1.7 nb, and 1.8 nb, respectively, and the corresponding fusion-evaporation reactions are $^{209}Bi(^{40}Ca, 4n)\,^{245}Lr$, $^{209}Bi(^{40}Ca, 3n)\,^{246}Lr$, $^{203}Tl(^{46}Ti, 2n)\,^{247}Lr$, $^{203}Tl(^{48}Ti, 3n)\,^{248}Lr$, $^{203}Tl(^{48}Ti, 2n)\,^{249}Lr$, and $^{209}Bi(^{44}Ca, 3n)\,^{250}Lr$.

ACKNOWLEDGMENTS

This work was supported by the Guangxi Natural Science Foundation under Grant No. 2022GXNSFBA035549, the Guangxi Science and Technology Base and Special Talent Program (Grant No. 2021AC19266), and the Open Project of Guangxi Key Laboratory of Nuclear Physics and Nuclear Technology under Grant No. NLK2022-01.

[1] S. Hofmann, Radiochim. Acta **99**, 405 (2011).

[2] C. E. Düllmann, M. Block, F. P. Heßberger, J. Khuyagbaatar, B. Kindler, J. V. Kratz, B. Lommel, G. Münzenberg, V. Pershina, D. Renisch, M. Schädel, and A. Yakushev, Radiochim. Acta **110**, 417 (2022).

[3] Y. T. Oganessian, Radiochim. Acta **99**, 429 (2011).

[4] Y. T. Oganessian and V. K. Utyonkov, Rep. Prog. Phys. **78**, 036301 (2015).

[5] T. Cap, M. Kowal, and K. Siwek-Wilczyńska, Eur. Phys. J. A **58**, 231 (2022).

[6] Y. T. Oganessian, F. S. Abdullin, P. D. Bailey, D. E. Benker, M. E. Bennett, S. N. Dmitriev, J. G. Ezold, J. H. Hamilton, R. A. Henderson, M. G. Itkis, Y. V. Lobanov, A. N. Mezentsev, K. J. Moody, S. L. Nelson, A. N. Polyakov, C. E. Porter, A. V. Ramayya, F. D. Riley, J. B. Roberto, M. A. Ryabinin *et al.*, Phys. Rev. Lett. **104**, 142502 (2010).

[7] Y. T. Oganessian, F. S. Abdullin, S. N. Dmitriev, J. M. Gostic, J. H. Hamilton, R. A. Henderson, M. G. Itkis, K. J. Moody, A. N. Polyakov, A. V. Ramayya, J. B. Roberto, K. P. Rykaczewski, R. N. Sagaidak, D. A. Shaughnessy, I. V. Shirokovsky, M. A. Stoyer, N. J. Stoyer, V. G. Subbotin, A. M. Sukhov, Y. S. Tsyganov *et al.*, Phys. Rev. C **87**, 014302 (2013).

[8] Y. T. Oganessian, F. S. Abdullin, C. Alexander, J. Binder, R. A. Boll, S. N. Dmitriev, J. Ezold, K. Felker, J. M. Gostic, R. K. Grzywacz, J. H. Hamilton, R. A. Henderson, M. G. Itkis, K. Miernik, D. Miller, K. J. Moody, A. N. Polyakov, A. V. Ramayya, J. B. Roberto, M. A. Ryabinin *et al.*, Phys. Rev. C **87**, 054621 (2013).

[9] V. K. Utyonkov, N. T. Brewer, Y. T. Oganessian, K. P. Rykaczewski, F. S. Abdullin, S. N. Dmitriev, R. K. Grzywacz, M. G. Itkis, K. Miernik, A. N. Polyakov, J. B. Roberto, R. N. Sagaidak, I. V. Shirokovsky, M. V. Shumeiko, Y. S. Tsyganov, A. A. Voinov, V. G. Subbotin, A. M. Sukhov, A. V. Sabel'nikov, G. K. Vostokin *et al.*, Phys. Rev. C **92**, 034609 (2015).

[10] Y. T. Oganessian and V. K. Utyonkov, Nucl. Phys. A **944**, 62 (2015).

[11] S. Hofmann, D. Ackermann, S. Antalic, H. G. Burkhard, V. F. Comas, R. Dressler, Z. Gan, S. Heinz, J. Heredia, F. P. Heßberger, J. Khuyagbaatar, B. Kindler, I. Kojouharov, P. Kuusiniemi, M. Leino, B. Lommel, R. Mann, G. Münzenberg, K. Nishio, A. G. Popeko *et al.*, Eur. Phys. J. A **32**, 251 (2007).

[12] L. Stavsetra, K. E. Gregorich, J. Dvorak, P. A. Ellison, I. Dragojević, M. A. Garcia, and H. Nitsche, Phys. Rev. Lett. **103**, 132502 (2009).

[13] C. E. Düllmann, M. Schädel, A. Yakushev, A. Türler, K. Eberhardt, J. V. Kratz, D. Ackermann, L.-L. Andersson, M. Block, W. Brüchle, J. Dvorak, H. G. Essel, P. A. Ellison, J. Even, J. M. Gates, A. Gorshkov, R. Graeger, K. E. Gregorich, W. Hartmann, R.-D. Herzberg *et al.*, Phys. Rev. Lett. **104**, 252701 (2010).

[14] J. M. Gates, C. E. Düllmann, M. Schädel, A. Yakushev, A. Türler, K. Eberhardt, J. V. Kratz, D. Ackermann, L.-L. Andersson, M. Block, W. Brüchle, J. Dvorak, H. G. Essel, P. A. Ellison, J. Even, U. Forsberg, J. Gellanki, A. Gorshkov, R. Graeger, K. E. Gregorich *et al.*, Phys. Rev. C **83**, 054618 (2011).

[15] S. Hofmann, S. Heinz, R. Mann, J. Maurer, J. Khuyagbaatar, D. Ackermann, S. Antalic, W. Barth, M. Block, H. G. Burkhard, V. F. Comas, L. Dahl, K. Eberhardt, J. Gostic, R. A. Henderson, J. A. Heredia, F. P. Heßberger, J. M. Kenneally, B. Kindler, I. Kojouharov *et al.*, Eur. Phys. J. A **48**, 62 (2012).

[16] J. Khuyagbaatar, A. Yakushev, C. E. Düllmann, D. Ackermann, L.-L. Andersson, M. Asai, M. Block, R. A. Boll, H. Brand, D. M. Cox, M. Dasgupta, X. Derkx, A. Di Nitto, K. Eberhardt, J. Even, M. Evers, C. Fahlander, U. Forsberg, J. M. Gates, N. Gharibyan *et al.*, Phys. Rev. Lett. **112**, 172501 (2014).

[17] S. Hofmann, S. Heinz, R. Mann, J. Maurer, G. Münzenberg, S. Antalic, W. Barth, H. G. Burkhard, L. Dahl, K. Eberhardt, R. Grzywacz, J. H. Hamilton, R. A. Henderson, J. M. Kenneally, B. Kindler, I. Kojouharov, R. Lang, B. Lommel, K. Miernik, D. Miller *et al.*, Eur. Phys. J. A **52**, 180 (2016).

[18] Z. Ren, B. Chen, Z. Ma, and G. Xu, Phys. Rev. C **53**, R572 (1996).

[19] L. Satpathy and S. Patra, Nucl. Phys. A **722**, C24 (2003).

[20] Z. Kalaninová, S. Antalic, A. N. Andreyev, F. P. Heßberger, D. Ackermann, B. Andel, L. Bianco, S. Hofmann, M. Huyse, B. Kindler, B. Lommel, R. Mann, R. D. Page, P. J. Sapple, J. Thomson, P. Van Duppen, and M. Venhart, Phys. Rev. C **89**, 054312 (2014).

[21] J. Konki, J. Khuyagbaatar, J. Uusitalo, P. Greenlees, K. Auranen, H. Badran, M. Block, R. Briselet, D. Cox, M. Dasgupta, A. Di Nitto, C. Düllmann, T. Grahn, K. Hauschild, A. Herzán, R.-D. Herzberg, F. Heßberger, D. J. Hinde, R. Julin, S. Juutinen *et al.*, Phys. Lett. B **764**, 265 (2017).

[22] J. L. Pore, J. M. Gates, R. Orford, C. M. Campbell, R. M. Clark, H. L. Crawford, N. E. Esker, P. Fallon, J. A. Gooding, J. T. Kwarsick, A. O. Macchiavelli, C. Morse, D. Rudolph, A. Såmark-Roth, C. Santamaria, R. S. Shah, and M. A. Stoyer, Phys. Rev. Lett. **124**, 252502 (2020).

[23] F. P. Heßberger, M. Block, C. E. Düllmann, A. Yakushev, M. Leino, and J. Uusitalo, Phys. Rev. Lett. **126**, 182501 (2021).
[24] I. Čeliković, M. Lewitowicz, R. Gernhäuser, R. Krücken, S. Nishimura, H. Sakurai, D. Ahn, H. Baba, B. Blank, A. Blazhev, P. Boutachkov, F. Browne, G. de France, P. Doornenbal, T. Faestermann, Y. Fang, N. Fukuda, J. Giovinazzo, N. Goel, M. Górska *et al.*, Phys. Rev. Lett. **116**, 162501 (2016).
[25] I. Ahmad, A. M. Friedman, R. R. Chasman, and S. W. Yates, Phys. Rev. Lett. **39**, 12 (1977).
[26] A. Chatillon, C. Theisen, P. T. Greenlees, G. Auger, J. E. Bastin, E. Bouchez, B. Bouriquet, J. M. Casandjian, R. Cee, E. Clément, R. Dayras, G. de France, R. de Toureil, S. Eeckhaudt, A. Görgen, T. Grahn, S. Grévy, K. Hauschild, R. D. Herzberg, P. J. C. Ikin *et al.*, Eur. Phys. J. A **30**, 397 (2006).
[27] T. Huang, D. Seweryniak, B. B. Back, P. C. Bender, M. P. Carpenter, P. Chowdhury, R. M. Clark, P. A. Copp, X.-T. He, R. D. Herzberg, D. E. M. Hoff, H. Jayatissa, T. L. Khoo, F. G. Kondev, G. Morgan, C. Morse, A. Korichi, T. Lauritsen, C. Müller-Gatermann, D. H. Potterveld *et al.*, Phys. Rev. C **106**, L061301 (2022).
[28] Y. T. Oganessian, A. Demin, N. Danilov, G. Flerov, M. Ivanov, A. Iljinov, N. Kolesnikov, B. Markov, V. Plotko, and S. Tretyakova, Nucl. Phys. A **273**, 505 (1976).
[29] F. P. Heßberger, G. Münzenberg, S. Hofmann, Y. K. Agarwal, K. Poppensieker, W. Reisdorf, K. H. Schmidt, J. R. H. Schneider, W. F. W. Schneider, H. J. Schött, P. Armbruster, B. Thuma, C. C. Sahm, and D. Vermeulen, Z. Phys. A **322**, 557 (1985).
[30] G. Flerov, Y. Korotkin, V. Mikheev, M. Miller, S. Polikanov, and V. Stchegolev, Nucl. Phys. A **106**, 476 (1967).
[31] A. Ghiorso, T. Sikkeland, A. E. Larsh, and R. M. Latimer, Phys. Rev. Lett. **6**, 473 (1961).
[32] G. Flerov, Y. Oganesian, Y. Lobanov, Y. Lasarev, S. Tretiakova, I. Kolesov, and V. Plotko, Nucl. Phys. A **160**, 181 (1971).
[33] K. Eskola, P. Eskola, M. Nurmia, and A. Ghiorso, Phys. Rev. C **4**, 632 (1971).
[34] M. Schadel, W. Brüchle, M. Brügger, H. Gaggeler, K. J. Moody, D. Schardt, K. Sümmerer, E. K. Hulet, A. D. Dougan, R. J. Dougan, J. H. Landrum, R. W. Lougheed, J. F. Wild, and G. D. O'Kelley, Phys. Rev. C **33**, 1547 (1986).
[35] Y. T. Oganessian, V. K. Utyonkov, N. D. Kovrizhnykh, F. S. Abdullin, S. N. Dmitriev, D. Ibadullayev, M. G. Itkis, D. A. Kuznetsov, O. V. Petrushkin, A. V. Podshibiakin, A. N. Polyakov, A. G. Popeko, R. N. Sagaidak, L. Schlattauer, I. V. Shirokovski, V. D. Shubin, M. V. Shumeiko, D. I. Solovyev, Y. S. Tsyganov, A. A. Voinov *et al.*, Phys. Rev. C **106**, L031301 (2022).
[36] V. A. Druin, Sov. J. Nucl. Phys. **12**, 146 (1971).
[37] E. D. Donets, V. A. Shchegolev, and V. A. Ermakov, Sov. At. Energy **19**, 995 (1965).
[38] E. K. Hulet, Results from heavy-ion bombardments of ^{254}Es, Technical Report.
[39] E. K. Hulet, New, heavy transuranium isotopes, Technical Report.
[40] F. P. Heßberger, S. Hofmann, D. Ackermann, V. Ninov, M. Leino, G. Münzenberg, S. Saro, A. Lavrentev, A. Popeko, A. Yeremin, and C. Stodel, Eur. Phys. J. A **12**, 57 (2001).
[41] G. Münzenberg, S. Hofmann, F. P. Heßberger, W. Reisdorf, K. H. Schmidt, J. H. R. Schneider, P. Armbruster, C. C. Sahm, and B. Thuma, Z. Phys. A **300**, 107 (1981).
[42] Z.-Q. Feng, F.-S. Zhang, G.-M. Jin, and X. Huang, Nucl. Phys. A **750**, 232 (2005).
[43] Z.-Q. Feng and G.-M. Jin, Phys. Rev. C **80**, 037601 (2009).
[44] Y. Engel, D. Brink, K. Goeke, S. Krieger, and D. Vautherin, Nucl. Phys. A **249**, 215 (1975).
[45] A. S. Umar and V. E. Oberacker, Phys. Rev. C **74**, 024606 (2006).
[46] P. Bonche, B. Grammaticos, and S. Koonin, Phys. Rev. C **17**, 1700 (1978).
[47] C. Shen, G. Kosenko, and Y. Abe, Phys. Rev. C **66**, 061602(R) (2002).
[48] G. Adamian, N. Antonenko, W. Scheid, and V. Volkov, Nucl. Phys. A **633**, 409 (1998).
[49] G. G. Adamian, N. V. Antonenko, and W. Scheid, Phys. Rev. C **68**, 034601 (2003).
[50] Z.-Q. Feng, G.-M. Jin, F. Fu, and J.-Q. Li, Nucl. Phys. A **771**, 50 (2006).
[51] G. Zhang, C. A. T. Sokhna, Z. Liu, and F.-S. Zhang, Phys. Rev. C **100**, 024613 (2019).
[52] D. Naderi, J. Phys. G: Nucl. Part. Phys. **40**, 125103 (2013).
[53] P. Fröbrich and I. Gontchar, Phys. Rep. **292**, 131 (1998).
[54] P. Fröbrich and S. Xu, Nucl. Phys. A **477**, 143 (1988).
[55] C. Li, F. Zhang, J. Li, L. Zhu, J. Tian, N. Wang, and F.-S. Zhang, Phys. Rev. C **93**, 014618 (2016).
[56] N. Wang, Z. Li, and X. Wu, Phys. Rev. C **65**, 064608 (2002).
[57] N. Wang, Z. Li, X. Wu, J. Tian, Y. X. Zhang, and M. Liu, Phys. Rev. C **69**, 034608 (2004).
[58] J. Aichelin, Phys. Rep. **202**, 233 (1991).
[59] B.-A. Bian, F.-S. Zhang, and H.-Y. Zhou, Nucl. Phys. A **829**, 1 (2009).
[60] M. Papa, T. Maruyama, and A. Bonasera, Phys. Rev. C **64**, 024612 (2001).
[61] Y.-H. Zhang, G. Zhang, J.-J. Li, Z. Liu, A. V. Yeremin, and F.-S. Zhang, Phys. Rev. C **106**, 014625 (2022).
[62] V. Weisskopf, Phys. Rev. **52**, 295 (1937).
[63] N. Bohr and J. A. Wheeler, Phys. Rev. **56**, 426 (1939).
[64] S. Cohen and W. J. Swiatecki, Ann. Phys. **22**, 406 (1963).
[65] W. Myers and W. Swiatecki, Ann. Phys. **84**, 186 (1974).
[66] V. E. Viola and T. Sikkeland, Phys. Rev. **128**, 767 (1962).
[67] A. J. Pacheco, J. O. Fernández Niello, D. E. DiGregorio, M. di Tada, J. E. Testoni, Y. Chan, E. Chávez, S. Gazes, E. Plagnol, and R. G. Stokstad, Phys. Rev. C **45**, 2861 (1992).
[68] J. Péter, C. Ngô, and B. Tamain, Nucl. Phys. A **250**, 351 (1975).
[69] H. W. Gäggeler, D. T. Jost, A. Türler, P. Armbruster, W. Brüchle, H. Folger, F. P. Heßberger, S. Hofmann, G. Münzenberg, V. Ninov, W. Reisdorf, M. Schädel, K. Sümmerer, J. V. Kratz, U. Scherer, and M. E. Leino, Nucl. Phys. A **502**, 561 (1989).